Interlayer coupling driven rotation of the magnetic easy axis in MnSe₂ monolayers and bilayers

Zhongqin Zhang,[1,2,3,*] Cong Wang,[2,3,*,†] Peng-Jie Guo,[2,3] Linwei Zhou,[2,3] Yuhao Pan,[2,3,4] Zhixin Hu ⦿,[1,‡] and Wei Ji ⦿[2,3,§]

[1]*Center for Joint Quantum Studies and School of Physics, Tianjin University, Tianjin 300350, China*

[2]*Beijing Key Laboratory of Optoelectronic Functional Materials and Micro-Nano Devices, School of Physics,*
Renmin University of China, Beijing 100872, China

[3]*Key Laboratory of Quantum State Construction and Manipulation (Ministry of Education),*
Renmin University of China, Beijing 100071, China

[4]*China North Artificial Intelligence and Innovation Research Institute, Beijing 100071, China*

Interlayer coupling plays a critical role in tuning the electronic structures and magnetic ground states of two-dimensional materials, influenced by the number of layers, interlayer distances, and stacking order. However, its effect on the orientation of the magnetic easy axis remains underexplored. In this study, we demonstrate that interlayer coupling can significantly alter the magnetic easy-axis orientation, as shown by the magnetic easy axis of monolayer $1T$-MnSe₂ tilting 67° from the z axis, while aligning with the z axis in the bilayer. This change results from variations in orbital occupations near the Fermi level, particularly involving nonmetallic Se atoms. Contrary to the traditional focus on magnetic metal atoms, our findings reveal that Se orbitals play a key role in influencing the easy-axis orientation and topological Chern numbers. Furthermore, we validate our conclusions by changing stacking orders, introducing charge doping, applying in-plane biaxial strains, and substituting nonmetallic atoms. Our results highlight the pivotal role of interlayer coupling in tuning the magnetic properties of layered materials, with important implications for spintronic applications.

I. INTRODUCTION

Two-dimensional (2D) van der Waals (vdW) magnetic materials have garnered significant attention and have achieved notable advancements in recent years [1,2], emerging as a promising platform for both fundamental research [3,4] and potential spintronics applications [5,6]. The magnetic properties of these materials are typically characterized by magnetization [7–9], magnetic orders [2,10,11], and magnetic anisotropy [10,12,13], with the latter two being easily tunable. Extensive discussions have been conducted on both in-plane and out-of-plane magnetic orders, associated net magnetization values, and their manipulation mechanisms for 2D magnets. In addition to these properties, magnetic anisotropy plays a pivotal role in sustaining long-range magnetic orders in 2D magnets at finite temperatures [3,4]. It is also closely associated with magnetic coercivity, a critical parameter determining whether the material behaves as a hard or soft magnet [14–16]. However, results on the magnetic easy axis are, unlike the magnetic order, available only for a limited number of 2D magnets, such as CrTe₂ [10,17,18]. This limitation in understanding hinders us from grasping the factors that could affect magnetic anisotropy, thereby limiting the development of effective strategies for modulating magnetic anisotropy.

The magnetic anisotropy was demonstrated to be tunable under various external stimuli, such as electric fields [19–21] and charge doping [22,23], which primarily change the filling of d orbitals of magnetic metal atoms. However, such tunability typically requires high stimulating strengths, which can lead to magnetic-order transitions [24,25] or irreversible structural phase transitions [26–29]. Thus, it is of paramount importance to explore gentle and sustainable mechanisms for rotating the magnetic easy-axis direction without introducing transitions of magnetic order or atomic structures. The ability to modulate various properties through interlayer coupling is one of the most striking features of 2D materials [1–3]. In 2D magnets, many demonstrations highlight the role of interlayer coupling in manipulating interlayer or intralayer magnetic order [30–34]. Although the orientation of the magnetic easy axis was observed to vary upon changing the number of layers in $1T$-CrTe₂ [17,18] and alpha-RuCl₃ [35], these systems also exhibit synchronous magnetic-order transition or structural symmetry breaking with layer number variation. The question of whether interlayer coupling can tune magnetic anisotropy independently remains largely unexplored.

In this paper, we theoretically explored the ability and mechanism to tune the magnetic easy axis in prototypic MnSe₂ mono- and bilayers via interlayer coupling using density-functional theory (DFT) calculations. We found that the magnetic easy axis rotates from 67° off the z axis in the monolayer to the z axis in the bilayer, without any transition of magnetic orders or atomic structures. By analyzing the contribution of each individual atom and orbital to the magnetic anisotropy energy (MAE), we identified that the

---

*These authors contributed equally to this work.

†Contact author: wcphys@ruc.edu.cn

‡Contact author: zhixin.hu@tju.edu.cn

§Contact author: wji@ruc.edu.cn

electron occupation of Se p orbitals is critical in driving this rotation. A comparison of the electronic band structures of the mono- and bilayers reveals the mechanism behind the occupation changes and the subsequent magnetic easy-axis rotation through interlayer electronic couplings upon stacking. This mechanism was further validated by tuning the occupation using other external stimuli such as stacking-order changes, electron or hole doping, in-plane biaxial strains, and substitution of nonmetallic atoms. Additionally, we observed that the Chern number of electronic bands near the Fermi level varies in response to the rotating magnetic moments and/or layer stacking, demonstrating ability to manipulate topological properties of these electronic states through various external stimuli.

II. METHODS

Our DFT calculations were performed using the generalized gradient approximation for the exchange-correlation potential in the form of Perdew-Burke-Ernzerhof (PBE) [36], the projector augmented-wave method [37], and a plane-wave basis set as implemented in the Vienna *Ab initio* Simulation Package (VASP) [38]. We also included the dispersion correction through Grimme's semiempirical D3 scheme [39] in combination with the PBE functional (PBE-D3). This combination yields accuracy comparable to that of the optB86b-vdW functional for describing geometric properties of layered materials (Appendix A, Tables III and IV) [40], but at a lower computational cost. To, accurately calculate the atomic structures, electronic structure, and MAE, kinetic energy cutoffs of 800 and 600 eV for the plane-wave basis were adopted for structural relaxations and electronic structure calculations, respectively. The shape and volume of $MnSe_2$ with ferromagnetic configuration was fully optimized and all atoms were allowed to relax until the residual force per atom was less than 0.01 eV/Å. Vacuum layers of 22 Å for monolayers and 18 Å for bilayers were employed to reduce imaging interactions between adjacent supercells. A Gamma-centered k mesh of $21 \times 21 \times 1$ was used to sample the first Brillouin zone of the unit cell for $MnSe_2$. The Gaussian smearing method with a σ value of 0.01 eV was applied for structural relaxation and electronic structure calculations. For accurate MAE calculations, the tetrahedron method with Blöchl corrections and a Gamma-centered $29 \times 29 \times 1$ k-mesh was employed. The onsite Coulomb interaction for Mn d orbitals was characterized by U and J values of 4.0 and 0.7 eV [41], respectively, as determined via a linear response method [42] and validated by the convergence of theoretical predictions (Appendix A, Fig. 6). A $2 \times 2\sqrt{3}$ supercell and four (eight) magnetic configurations (Appendix B) were considered to identify the magnetic ground state for the monolayer (bilayer). Spin-exchange coupling parameters were extracted based on an anisotropic nearest-neighbor Heisenberg model; please refer to Appendix C for details.

The Atomic-orbital Based *Ab initio* Computation at USTC (ABACUS) package [43,44] and PYATB [45] were used to calculate the Chern numbers. By using the WANNIER90 package, we constructed the tight-binding model of $MnSe_2$ with both Mn $3d$ and Se $4p$ orbitals based on the maximally localized Wannier functions method [46]. We further plotted edge states

and verified our conclusions regarding topological transitions using the WANNIERTOOLS software package [47].

Direct charge doping was applied to Se atoms using the ionic-potential method [48]. Specifically, electrons (or holes) were extracted from a $3d$ core level of Se and placed into the lowest unoccupied band of $MnSe_2$. This method ensures that the doped charges remain localized around the Se atoms while maintaining the neutrality of the layer. In-plane biaxial strain was simulated on the monolayer $MnSe_2$, which was fully relaxed in the ferromagnetic configuration. The in-plane lattice vectors of the equilibrium structure were compressed or stretched to simulate strain. During relaxations, all atoms were allowed to relax while the in-plane lattice constants remained fixed.

The spin-orbit coupling was considered in all calculations carried out to determine the magnetic easy-axis directions. The magnetic easy axis was identified using the Renmin Magnetic Easy Axis Finder (REMEAF) toolkit [49], which utilizes the simulated annealing algorithm and invokes VASP to determine the global easy-axis orientation. We calculated MAEs for certain angles and used linear interpolation to generate the continuous plots of the angular dependence of the MAE.

Spin-exchange coupling parameters were extracted based on the Heisenberg model as follows:

$$H = H_0 - J_1 \sum_{\langle i \neq j \rangle} \overrightarrow{S_i} \cdot \overrightarrow{S_j} - J_2 \sum_{\langle\langle i \neq j \rangle\rangle} \overrightarrow{S_i} \cdot \overrightarrow{S_j} - J_3 \sum_{\langle\langle\langle i \neq j \rangle\rangle\rangle} \overrightarrow{S_i}$$
$$\cdot \overrightarrow{S_j} - J_4 \sum_{\langle i, j \rangle} \overrightarrow{S_i} \cdot \overrightarrow{S_j} - J_5 \sum_{\langle\langle i, j \rangle\rangle} \overrightarrow{S_i} \cdot \overrightarrow{S_j}$$
$$- J_6 \sum_{\langle\langle\langle i, j \rangle\rangle\rangle} \overrightarrow{S_i} \cdot \overrightarrow{S_j}.$$

Here, $J_1 \sim J_3$ and $J_4 \sim J_6$ represent the first-, second-, and third-nearest intra- and interlayer couplings, respectively, as illustrated in Figs. 1(a)–1(c). Here, we present the method for extracting the monolayer exchange constants J_1, J_2, and J_3, while the corresponding method for the bilayer is detailed in Appendix B. We derived the spin exchange parameters from the total energy differences of the four magnetic configurations shown in Figs. 6(a)–6(d). The magnetic energy contributions of these magnetic configurations in each magnetic unit cell write as

$$E_a = -\frac{N^2}{4} \times \frac{1}{2}(6J_1 + 6J_2 + 6J_3) + E_0,$$

$$E_b = -\frac{N^2}{4} \times \frac{1}{2}(2J_1 - 2J_2 - 2J_3) + E_0,$$

$$E_c = -\frac{N^2}{4} \times \frac{1}{2}(-2J_1 - 2J_2 + 6J_3) + E_0,$$

$$E_d = -\frac{N^2}{4} \times \frac{1}{2}(-2J_1 + 2J_2 - 2J_3) + E_0,$$

where N represents the unpaired spins on each Mn atom, which is treated as 3 in our exchange parameter calculations, and E_0 represents the energy that is independent of the magnetic configuration. Then, by substituting the energies of the magnetic configurations (see Table V), we solved for the values of the exchange constants.
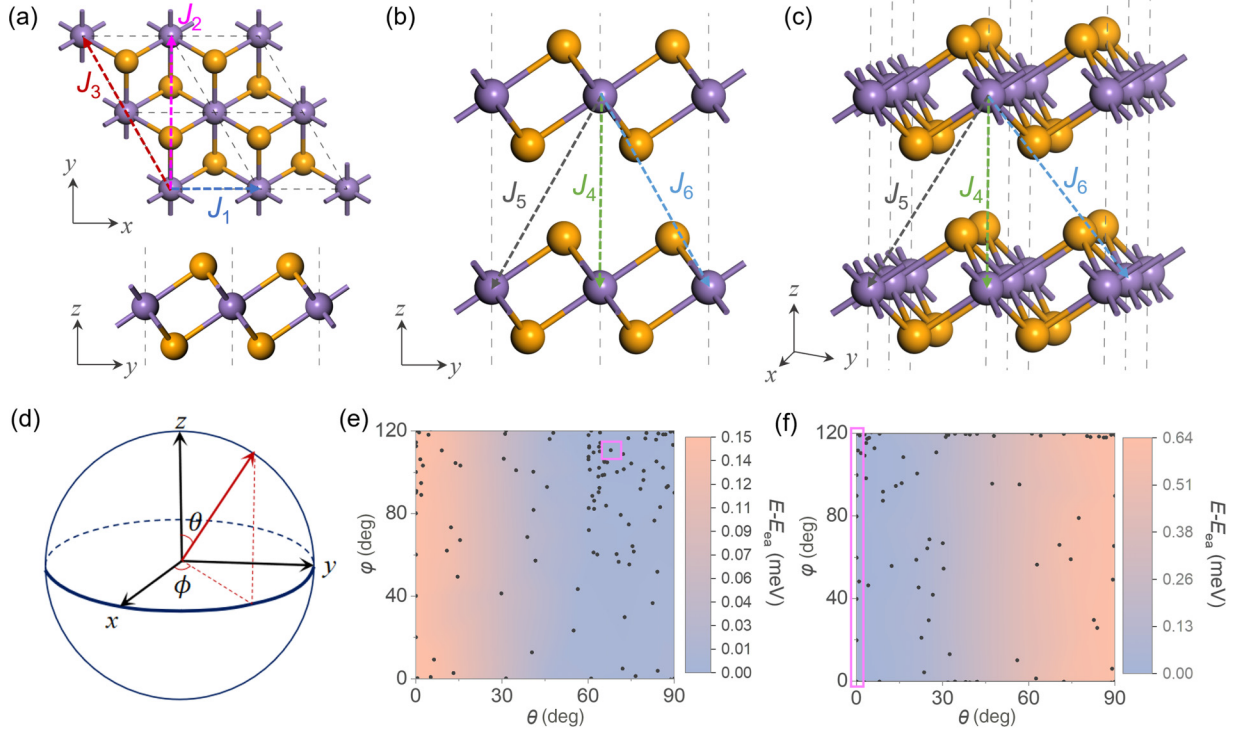
FIG. 1. Structure and easy axis of mono- and bilayer MnSe$_2$. (a) Top and side views of monolayer MnSe$_2$. Purple and orange balls represent Mn and Se atoms, respectively. Dashed arrows denote intralayer spin-exchange parameters J_1, J_2, and J_3 between Mn sites with different colors. (b), (c) Side and oblique view of an AA-stacked bilayer MnSe$_2$. Colored dashed arrows denote interlayer spin-exchange parameters J_4, J_5, and J_6 between Mn sites. (d) Definition of polar angle θ and azimuth angle φ in the spherical coordinate. (e), (f) Angular dependence of the calculated MAE of monolayer (e) and bilayer (f) MnSe$_2$. The total energy of the Mn moment oriented to the direction of easy axis was chosen as the zero-energy reference and marked by pink boxes. Black dots represent MAE results for angles calculated with DFT.

III. RESULTS AND DISCUSSION

A. Magnetic anisotropy in MnSe$_2$ monolayer and bilayer

Monolayer MnSe$_2$ crystallizes in a hexagonal $1T$ structure with space group P-$3M1$, as depicted in Fig. 1(a). Each Mn atom is octahedrally coordinated by six Se atoms, with Se-Mn-Se bond angle close to 90° (measured as either 90.96° or 89.04°), indicating minimal Jahn-Teller distortion. In the MnSe$_2$ bilayer, the AA stacking [Figs. 1(b) and 1(c)] is found to be over 4 meV/Mn more stable compared to other stacking configurations (Appendix D, Fig. 7 and Table VII). To determine intra- and interlayer magnetic ground state, we adopted the structure optimized with the ferromagnetic (FM) order and calculated relative energies of four (eight) magnetic configurations for monolayer (bilayer) MnSe$_2$ (see Appendix B for more details). We found that both the monolayer and the bilayer

exhibit a FM ground state, as indicated by the data listed in Table V, consistent with the theoretical predictions reported in the literature [30,50].

Three intralayer (J_1 to J_3) and three-interlayer (J_4 to J_6) spin-exchange coupling parameters, which are indicated by dashed arrows in different colors in Figs. 1(a)–1(c), were computed based on the Heisenberg model (seen in Sec. II, and Appendix B), with their values provided in Table I. Notably, the dominant and positive nearest-neighbor intralayer spin-exchange coupling J_1 (7.5 and 8.7 meV/Mn, respectively, for the mono- and bilayer) aligns with the energetically favored intralayer FM configuration. Comparable values for the interlayer spin exchanges, $J_4 = 3.6$ meV/Mn and $J_5 = 3.5$ meV/Mn, indicate that the interlayer FM coupling is as strong as the intralayer magnetic coupling in MnSe$_2$, which is prominent in layered magnetic materials [31,40,51].

TABLE I. Lattice constant, magnetic ground state, exchange parameters, and easy axis of MnSe$_2$. Magnetic anisotropy energy (MAE) is defined as the energy difference required to reorient the magnetic moment of MnSe$_2$ from its easy axis to hard axis.

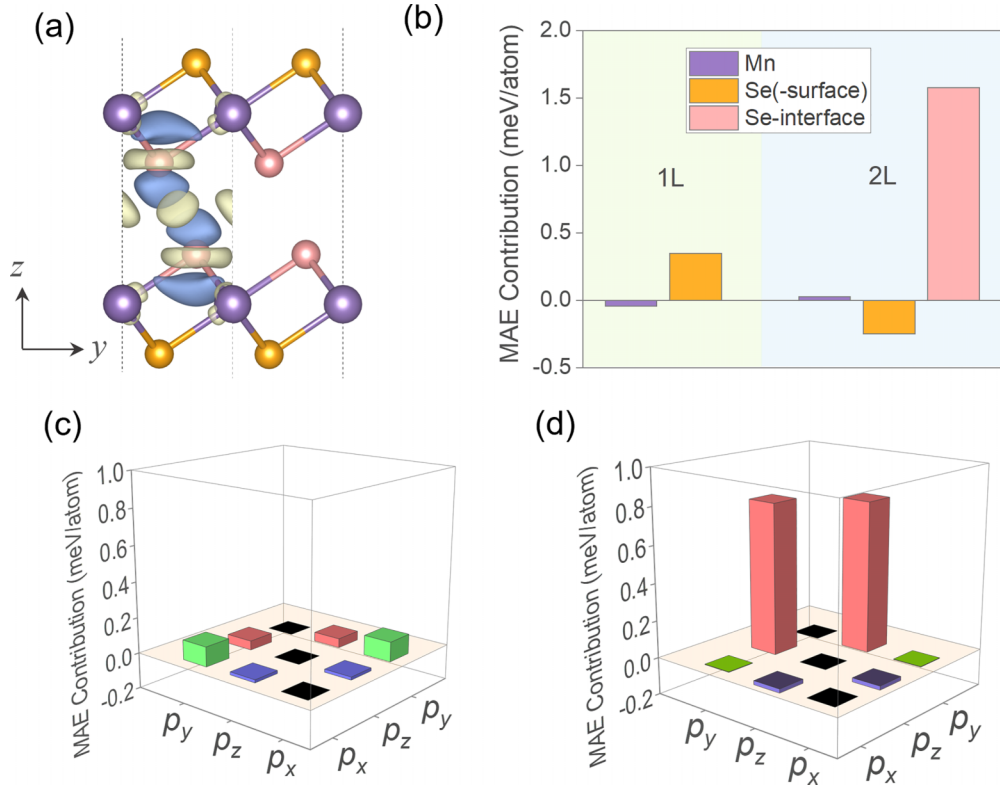| Layer number	Lattice constant (Å)	Mag. config.		Exchange parameters (meV/Mn)						Easy axis		MAE (meV/Mn)
		Intralayer	Interlayer	J_1	J_2	J_3	J_4	J_5	J_6	θ(deg)	φ(deg)	
1L	3.61	FM		7.5	1.2	0.2				67	111	0.2
2L	3.63	FM	FM	8.7	0.3	1.0	3.6	3.5	0.7	0		0.6

FIG. 2. (a) Side view of interlayer differential charge density (DCD) of bilayer MnSe$_2$ with an isosurface value of 0.0005 e/bohr^3. Light-yellow and blue isosurface indicates charge accumulation and reduction after layer stacking. Nonequivalent Se atoms in bilayer MnSe$_2$ are colored in orange and pink. (b) Atomically decomposed MAE contributions of monolayer (1L) and bilayer (2L) MnSe$_2$. (c), (d) Orbital-resolved MAE contributions of Se in monolayer (c) and Se interface in bilayer (d).

By considering the C_{3v} spatial symmetries of MnSe$_2$, a range of polar angle $\theta \in [0, 90°]$ and azimuth angle $\varphi \in [0, 120°]$ [Fig. 1(d)] covers all possible magnetic easy-axis orientations. Figure 1(e) shows the magnetic anisotropic energies of the MnSe$_2$ monolayer as the magnetization direction rotates with θ and φ, revealing an easy-axis orientation along $\theta = 67°$ and $\varphi = 111°$. When an additional layer is stacked onto the monolayer to form the bilayer, the easy axis rotates to align with the z axis [$\theta = 0$, Fig. 1(f)]. Such a substantial rotation of the magnetic easy-axis direction by adding a single layer to a monolayer in 2D layered magnetic materials warrants further exploration.

B. Origin of the interlayer-coupling tunable magnetic easy-axis direction

Figure 2(a) shows the interlayer differential charge density of the bilayer MnSe$_2$. Apparent charge reduction (blue contours) near the interlayer Se atoms (pink balls) and charge accumulation (light-yellow contours) primarily in the vdW gap region suggest strong interlayer electronic hybridization. Meanwhile, charge transfer on Mn and surface Se (orange balls) is less significant, indicating a weaker effect of interlayer coupling on them and thus a different contribution to the easy-axis rotation. To understand the role of interlayer coupling in rotating the easy axis, we decomposed the MAE contribution into individual atoms [Fig. 2(b)]. Here, positive and negative MAE contributions correspond to magnetic easy-

axis directions favoring the z axis and in-plane directions, respectively. In the MnSe$_2$ monolayer, all Se atoms are categorized as Se-surface atoms and contribute a positive MAE contribution (0.36 meV per atom), while Mn atoms donate a smaller negative contribution (-0.04 meV per atom), favoring an in-plane magnetic easy axis. The competition between these contributions results in the tilted orientation of the magnetic easy axis in the monolayer. After the stacking of an additional MnSe$_2$ layer, the MAE contributions for Mn and surface Se atoms change sign but have smaller absolute values (no more than 0.25 meV per atom). However, the Se-interface atoms exhibit a dominant positive MAE contribution (1.58 meV per atom), decisively outweighing the negative contribution from Se surface (-0.25 meV per atom), leading to the alignment of the magnetic easy axis with the z axis in the bilayer.

Therefore, we further focused on the origin of the different Se contributions to MAE across different numbers of layers and decomposed the MAE into Se p_x, p_y, and p_z orbitals for the mono- [Fig. 2(c)] and bilayer [Fig. 2(d) and Appendix F, Fig. 9(b)], namely,

$$\langle p_i | H_{\text{SOC}}(x) | p_j \rangle - \langle p_i | H_{\text{SOC}}(z) | p_j \rangle,$$

where $H_{\text{SOC}}(x)$ is the spin-orbit coupling Hamiltonian when the magnetic moment is oriented along the x direction, and the p_i, p_j represents p_x, p_y, or p_z orbitals. In the monolayer, all Se orbital contributions are relatively small, resulting in the moderate total contribution of 0.36 meV per atom. As
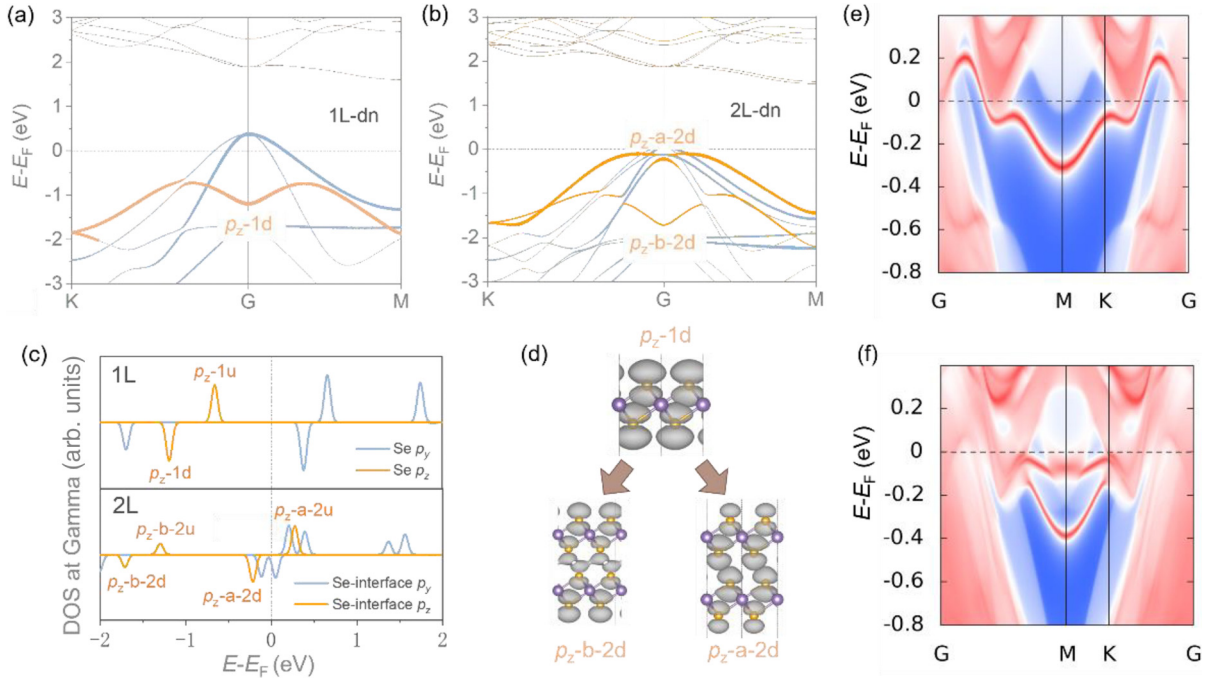
FIG. 3. Electronic structures of $MnSe_2$. (a), (b) Spin-down band structures of monolayer (a) and bilayer (b) $MnSe_2$. The p_z and p_y orbitals of (interfacial) Se are mapped with different colors in bands near the Fermi level: orange, p_z; light blue, p_y. The Fermi level is marked using gray dotted-dashed line. (c) Projected density of states for the p_y and p_z orbitals of (interfacial) Se at the Gamma point in monolayer (upper panel) and bilayer (lower panel). (d) Visualized wave-function norms for the labeled states in (a)–(c). The isosurface value is 0.0012 e/bohr^3. (e), (f) Surface states of monolayer (e) and bilayer (f) $MnSe_2$.

for the bilayer, the contribution from the p_z-p_y component of Se-interface atoms ($\sim$0.8 meV per atom) is significantly prominent and at least an order of magnitude larger than other components (less than 0.03 meV per atom). This result indicates that the interaction between the p_z and p_y orbitals of the Se-interface atoms is crucial in orienting the magnetic easy axis toward the normal direction in the $MnSe_2$ bilayer. This finding provides a different perspective from the prevailing view in the literature, which attributes easy-axis reorientation primarily to the influence of metallic atoms. Previous literature have demonstrated significant contributions of nonmetallic atoms to magnetic anisotropy in 2D magnets [52–54], our work further shows that their interlayer coupling significantly influences the direction of the easy magnetic axis.

To understand the origin of the pronounced p_z-p_y component, we mapped the orbitals of (interfacial) Se on the band structures of both monolayer and bilayer. The orbital decomposition and layer-number dependence of electronic band structures show qualitative consistency across different spin components. For clarity, we focused on the spin-down electronic structure here [Figs. 3(a) and 3(b)] and provide the spin-up results in Appendix G, Fig. 10. According to second-order perturbation theory [55], the states with different occupations near the Fermi level contribute most significantly to the MAE, primarily composed of p_z and p_y orbitals in both mono- and bilayer $MnSe_2$. For a clear comparison, we plot the projected density of states of Se p states at G point in Fig. 3(c). In the monolayer, the p_z states are distant from the Fermi level, resulting in an energy difference of approximately 0.85 eV between the p_z and p_y states with different occupations [Fig. 3(a) and the upper panel of Fig. 3(c)]. In the

bilayer, the interfacial Se p orbitals overlap and hybridize into bonding (p_z-b-2d) and antibonding (p_z-a-2d) states to release Pauli/Coulomb repulsions [Fig. 3(d)], significantly splitting the p_z bands. This reduces the energy differences between p_z and p_y states around the Fermi level with different occupation to 0.1 eV at the G point [Fig. 3(b) and the lower panel of Fig. 3(c)], thereby enhancing p_z-p_y interactions and increasing MAE contribution favoring the z axis [Fig. 2(d)].

We also explored the possibility that the differences in Kitaev interactions in the mono- and bilayer $MnSe_2$ might modulate the magnetic easy-axis direction. However, as listed in Appendix C, the noncollinear spin exchange and Kitaev interactions are at least two orders of magnitude weaker than the isotropic spin-exchange coupling J_1 and remain nearly unchanged with increasing layer number, indicating their negligible influence on the magnetic easy-axis direction in $MnSe_2$ mono- and few layers.

Furthermore, we found that monolayer and bilayer $MnSe_2$ are topologically nontrivial semimetals. We term the three energy bands crossing the Fermi level as band $N-1$, band N, and band $N+1$, respectively (Appendix H, Fig. 11). Forming interlayer bonding states directly modifies band structures near the Fermi level, while layer-number induced easy-axis rotation changes the magnetic group from P-1.1 in the monolayer to P-3m'1 in the bilayer, collectively leading to layer-number tunable Chern numbers and surface states [Table II and Figs. 3(e) and 3(f)]. Both magnetic anisotropy and topological properties are governed by the bands around the Fermi level, suggesting possible magnetic-field manipulated topological features. In addition to layer stacking, applying a vertical magnetic field can also reorient the mag-

TABLE II. Chern numbers of MnSe$_2$ in 1L and 2L with different numbers of occupied bands and directions of magnetic moments.

Layer number		1L		2L
Direction		Easy axis	z	Easy axis (z)
Band number	$N+1$	-4	-2	2
	N	0	0	0
	$N-1$	0	-4	-5

netic moments in the monolayer from the easy axis to the z axis, thereby altering the band structures and magnetic group (from P-1.1 to P-3m'1). This shift results in variations in the topological Chern numbers of the three nontrivial bands (Appendix H and Table II), similar to what is observed in CeX (X = Cl, Br, I) [56].

C. Modulation of the easy-axis direction in MnSe$_2$ monolayer

In addition to the magnetic field, stacking orders, charge doping, and external strain can also effectively change the electron band structure around the Fermi level and thus the easy-axis direction. Besides the most stable AA stacking, we considered five additional stacking orders and demonstrated that the interlayer stacking can effectively manipulate the magnetic ground state and easy-axis direction (Appendix D) [30]. The AB stacking configuration [Fig. 4(a)] shares the same FM ground state with AA stacking but exhibits a different in-plane easy axis. To understand how stacking order rotates the orientation of the easy axis, we plotted the contributions of different atoms to the MAE of both AA- and AB-stacked bilayers [Fig. 4(b)]. In the transition from AA to AB stacking, there is no qualitative change in the favored easy-axis direction of different atoms, but the MAE contribution of the Se interface decreases significantly by threefold, while the contribution of the Se surface nearly doubles. As a result, the reduced MAE contribution of the Se interface becomes less competitive compared to that of the Se surface, leading to an in-plane easy axis in the AB-stacked bilayer. This change in the Se-interface MAE contribution arises from the weakened interaction between the p_z and p_y states (Appendix I, Fig. 12).

Charge doping and in-plane strain are commonly introduced by substrates. They are often employed to manipulate the magnetism of 2D magnets. Therefore, we considered the influence of charge doping and in-plane strain on the magnetic anisotropy of monolayer MnSe$_2$. By varying doping concentrations [Fig. 4(c)] and applying biaxial strain [Fig. 4(d)], the orientations of the easy axis of monolayer MnSe$_2$ can be manipulated. When the doping concentration is adjusted to either -0.05 or 0.075 e/Se, or when biaxial strain reaches -2 or 2%, the easy axis undergoes a rotation towards the xy plane or z axis (Appendix I, Tables VIII and IX), showcasing the adjustability of the easy axis in monolayer MnSe$_2$. The atomically decomposed MAE in Figs. 4(c) and 4(d) re-
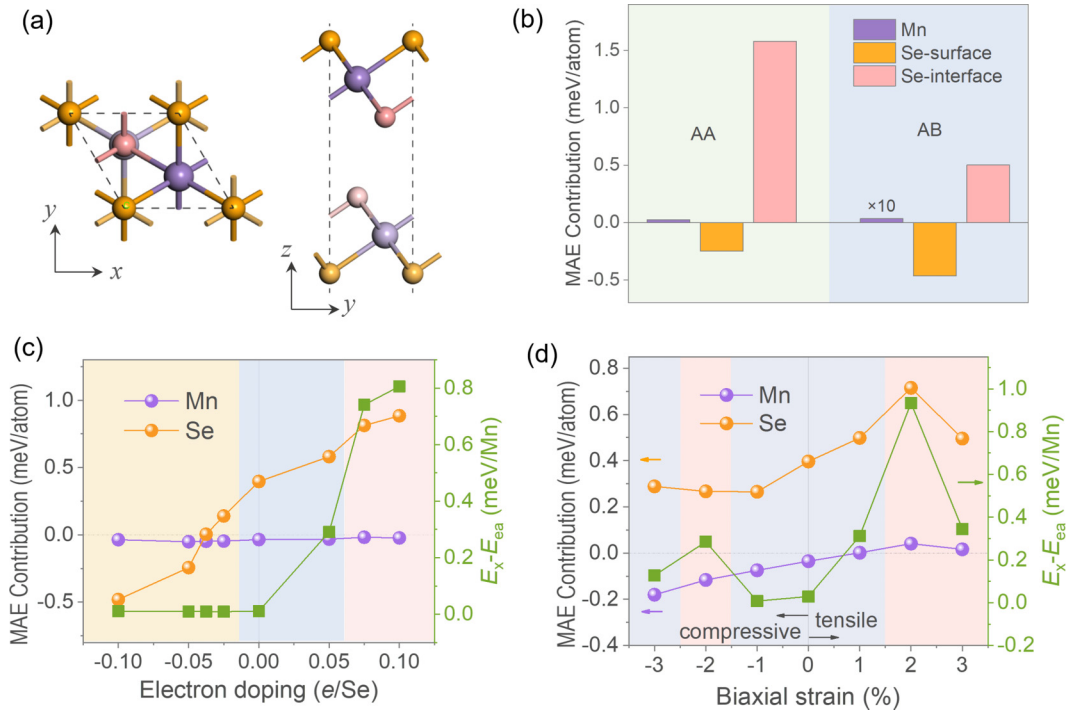

FIG. 4. Modulation of the magnetic anisotropy of MnSe$_2$. (a) Structure model of AB-stacked bilayer. (b) Atomically decomposed MAE of AA and AB stacking. (c), (d) Atomically decomposed MAE and the energy difference required to reorient the magnetic moments from the easy axis (E_{ea}) to the x axis (E_x) as a function of doping concentrations (c) and in-plane biaxial strain (d) in monolayer MnSe$_2$. The light-brown, blue, and pink shading indicates that the easy axis lies in the xy plane, tilts away from the z axis, and aligns with the z axis, respectively.

veals that the MAE contribution of Se exhibits significant variability, whereas Mn consistently makes relatively minor contributions, corroborating earlier findings.

Finally, to further support the importance of nonmetallic atoms in orientating the easy axis, we substituted the Se atoms with Te atoms and studied the magnetic anisotropy of monolayer $1T$-MnTe$_2$. The $1T$-MnTe$_2$ exhibits a large out-of-plane magnetic anisotropy with a MAE value of 1.6 meV/Mn, where the contribution from Te (1.7 meV per atom favoring the z axis) is much larger than that from Mn (-0.3 meV per atom). The difference in the easy axis and MAE between MnSe$_2$ and MnTe$_2$ again demonstrates the substantial contributions of nonmetallic atoms on tuning magnetic anisotropy in MnX_2.

IV. CONCLUSIONS

In summary, we found that MnSe$_2$ is a ferromagnetic topological semimetal, with its easy-axis direction and topological properties highly dependent on the electronic band structure near the Fermi level. By analyzing atomically and orbitally decomposed MAE and electronic structures, we revealed the mechanism by which interlayer coupling changes the direction of the easy axis from $67°$ off the z axis in the monolayer to the z axis in the bilayer. In MnSe$_2$, the electronic states near the Fermi level are mainly contributed by nonmetallic Se atoms, resulting in the significant influence of interlayer coupling between interfacial Se atoms on the electronic band structure. From the monolayer to bilayer, p_z orbitals of Se are split towards the Fermi level due to interlayer coupling, leading to the pronounced p_z-p_y interaction and MAE contribution favoring the z axis. Furthermore, based on the modification of Se electronic states, we demonstrated that the orientation of the magnetic easy axis can also be manipulated by stacking orders, doping, biaxial strain, and substitution of nonmetallic atoms. Our results might advance the understanding of the mechanism behind the rotation of the easy-axis orientation in 2D layered magnets.

APPENDIX A: EFFECTS OF FUNCTIONAL AND DIFFERENT U VALUES ON THE GEOMETRY AND MAGNETIC GROUND STATE OF MONOLAYER MnSe$_2$

To verify the reliability of our conclusion, we carried out the calculation with different exchange functionals and different vdW corrections as shown in Tables III and IV. We choose the PBE-D3+UJ for structure optimization and electronic structures calculations.

Additionally, we examined the effects of different on-site Coulomb U values. Our calculations indicate the ferromagnetic state is the magnetic ground state using U values of over 2 eV, which is consistent with experimental observations. By using the linear response method calculated-U value of 4 eV, our calculations indicate the magnetic ground states and geometric structures converge and should be robust in our calculations (Fig. 5).

TABLE III. Lattice constant, magnetic moment per Mn atom, and layer thickness d_1 of monolayer MnSe$_2$ calculated with different exchange-correlation functionals.

Functional	Lattice constant (Å)	Mag. Mn (μ_B)	d_1 (Å)
PBE-w/o UJ	3.48	2.89	2.87
PBE+UJ	3.62	3.71	2.86
PBE-D2+UJ	3.57	3.67	2.90
PBE-D3+UJ	3.61	3.71	2.88
optB86b-vdw+UJ	3.56	3.60	2.88
optB88-vdw+UJ	3.59	3.62	2.88
SCAN- rVV10+UJ	3.63	4.00	2.83

TABLE IV. Lattice constant, magnetic moment per Mn, layer thickness d_1, and interlayer spacing d_2 of bilayer MnSe$_2$ with various exchange-correlation functionals.

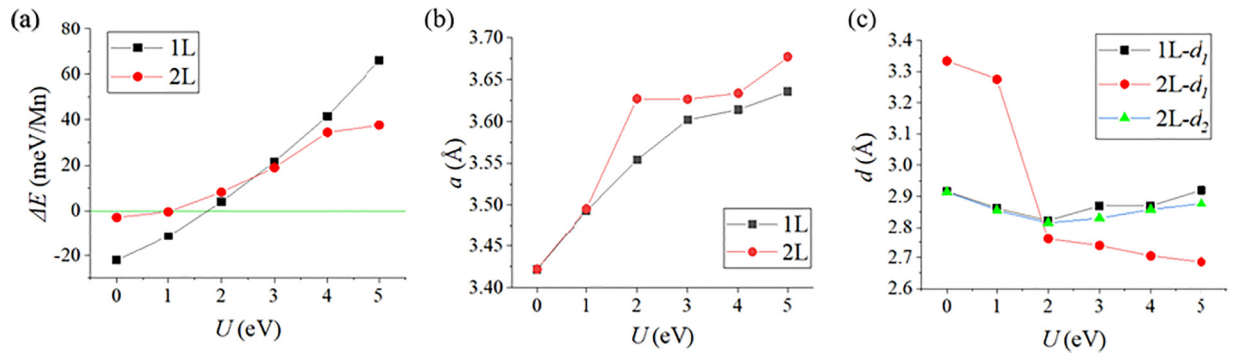| Functional	Lattice constant (Å)	Mag. Mn (μ_B)	d_1 (Å)	d_2 (Å)
PBE-w/o UJ	3.48	2.89	2.75	3.26
PBE+UJ	3.65	3.78	2.85	3.00
PBE-D2+UJ	3.59	3.74	2.91	2.91
PBE-D3+UJ	3.63	3.78	2.86	2.71
optB86b-vdw+UJ	3.59	3.70	2.88	2.70
optB88-vdw+UJ	3.62	3.72	2.88	2.81
SCAN-rVV10+UJ	3.67	4.07	2.80	2.78

FIG. 5. (a) Energy differences between FM and antiferromagnetic (AFM) configurations ($\Delta E = E_{AFM}\text{-}E_{FM}$), (b) lattice constant a, and (c) thickness d_1 and interlayer spacing d_2 with respect to different U values. Here, we choose the AFM configuration with lowest energy among all AFM orders in mono- or bilayer MnSe$_2$ as a representative.
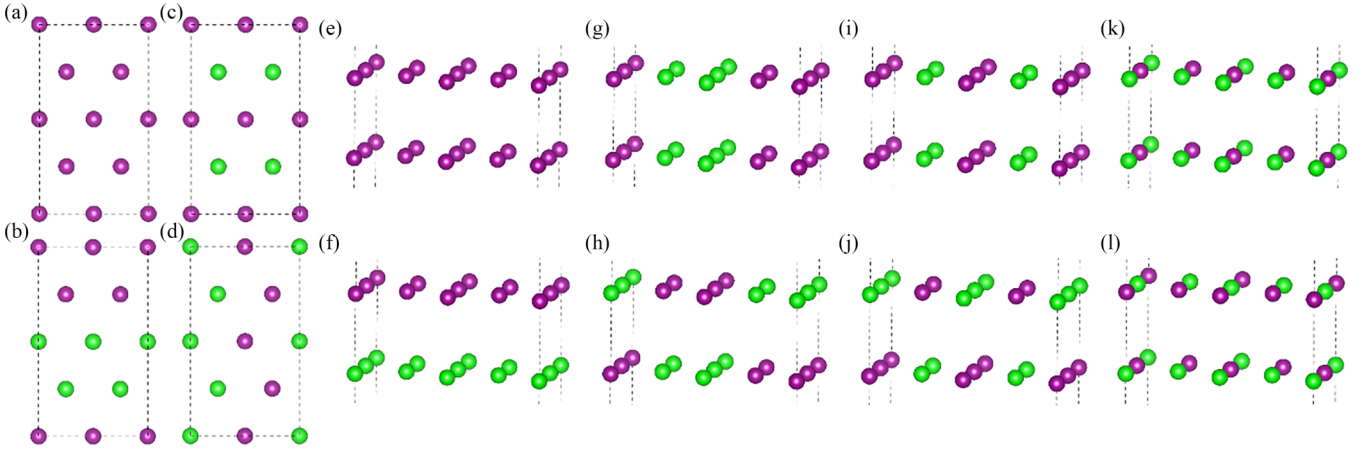
FIG. 6. Magnetic ground states and spin-exchange parameters of mono-/bilayer MnSe$_2$. (a)–(d) Top views of schematics showing intralayer magnetic orders, including FM (a), AABB (b), ABAB (c), and ZZ (d) in monolayer/bilayer MnSe$_2$, respectively. (e)–(l) Schematics of eight magnetic orders used for finding the magnetic ground state and deriving spin-exchange parameters of bilayer MnSe$_2$. Purple and green balls represent two antiparallel orientations of magnetic moments on Mn atoms, respectively.

APPENDIX B: MAGNETIC GROUND STATES AND HEISENBERG EXCHANGE PARAMETERS

Magnetic energies of these magnetic configurations in each magnetic unit cell read as follow:

$$E_e = -\frac{N^2}{4} \times \frac{1}{2}\left(6J_1 + 6J_2 + 6J_3 + \frac{1}{2}J_4 + 3J_5 + 3J_6\right) + E_0$$

$$E_f = -\frac{N^2}{4} \times \frac{1}{2}\left(6J_1 + 6J_2 + 6J_3 - \frac{1}{2}J_4 - 3J_5 - 3J_6\right) + E_0$$

$$E_g = -\frac{N^2}{4} \times \frac{1}{2}\left(2J_1 - 2J_2 - 2J_3 + \frac{1}{2}J_4 + J_5 - J_6\right) + E_0$$

$$E_h = -\frac{N^2}{4} \times \frac{1}{2}\left(2J_1 - 2J_2 - 2J_3 - \frac{1}{2}J_4 - J_5 + J_6\right) + E_0$$

$$E_i = -\frac{N^2}{4} \times \frac{1}{2}\left(-2J_1 - 2J_2 + 6J_3 + \frac{1}{2}J_4 - J_5 - J_6\right) + E_0$$

$$E_j = -\frac{N^2}{4} \times \frac{1}{2}\left(-2J_1 - 2J_2 + 6J_3 - \frac{1}{2}J_4 + J_5 + J_6\right) + E_0,$$

$$E_k = -\frac{N^2}{4} \times \frac{1}{2}\left(-2J_1 + 2J_2 - 2J_3 + \frac{1}{2}J_4 - J_5 + J_6\right) + E_0,$$

$$E_l = -\frac{N^2}{4} \times \frac{1}{2}\left(-2J_1 + 2J_2 - 2J_3 + \frac{1}{2}J_4 + J_5 - 3J_6\right) + E_0,$$

TABLE V. Relative total energies of mono-/bilayer MnSe$_2$ in different magnetic configurations shown in Fig. 6. The term "Mag. config." is the abbreviation of magnetic configuration. We set the total energy of the FM(-FM) configuration as the reference zero.

Layer number	Mag. config.	ΔE (meV/Mn)
Monolayer	FM	0.0
	AABB	42.0
	ABAB	77.7
	ZZ	70.3
Bilayer	FM-FM	0.0
	FM-AFM	31.4
	AABB-FM	62.1
	AABB-AFM	72.4
	ABAB-FM	100.4
	ABAB-AFM	94.9
	ZZ-FM	102.4
	ZZ-AFM	108.1

where N represents the unpaired spins on each Mn atom, which is treated as 3 in our exchange-parameter calculations, and E_0 represents the energy that is independent of the magnetic configuration.

APPENDIX C: ANISOTROPIC SPIN-EXCHANGE PARAMETERS AND KITAEV INTERACTIONS

To investigate the effects of noncollinear spin-exchange and Kitaev interactions on magnetic anisotropy, we considered an anisotropic Hamiltonian containing both anisotropic spin-exchange coupling and single-ion anisotropy terms:

$$H = H_{EX} + H_{SIA}$$
$$= -\frac{1}{2}\left[\sum_{i \neq j} \boldsymbol{S}_i \cdot \boldsymbol{J}_{ij} \cdot \boldsymbol{S}_j + 2\sum_i \boldsymbol{S}_i \cdot \boldsymbol{A} \cdot \boldsymbol{S}_i\right],$$

where $\boldsymbol{J}_{ij}$ is the anisotropic Heisenberg exchange parameter matrix and $\boldsymbol{A}$ is a vector representing the single-ion anisotropy. We assume that $\boldsymbol{J}_{ij}$ is symmetric and $\boldsymbol{A}_y = 0$. Following the methodology outlined in our previous research [40,57], we derived the parameters and transformed the $\boldsymbol{J}_{ij}$ matrix into the coordinate system $\{\alpha\beta\gamma\}$, corresponding to the Mn–Se bond directions. The resulting $\boldsymbol{J}_{ij}$ matrix is

$$\boldsymbol{J}_{ij} = \begin{pmatrix} 8.73 & -0.02 & 0.04 \\ -0.02 & 8.76 & 0.05 \\ 0.04 & 0.05 & 8.66 \end{pmatrix}$$

for the monolayer, and

$$\boldsymbol{J}_{ij} = \begin{pmatrix} 11.47 & 0.02 & 0.08 \\ 0.02 & 11.51 & 0.02 \\ 0.08 & 0.02 & 11.47 \end{pmatrix}$$

for the bilayer.

Because the nondiagonal elements are negligible in $\boldsymbol{J}_{ij}$, we can express the H_{EX} as

$$H_{EX} = -\frac{1}{2}\sum_{i \neq j}\left(\lambda_\alpha S_i^\alpha S_j^\alpha + \lambda_\beta S_i^\beta S_j^\beta + \lambda_\gamma S_i^\gamma S_j^\gamma\right)$$
$$= -\frac{1}{2}\sum_{i \neq j}\left(J\boldsymbol{S}_i \cdot \boldsymbol{S}_j + K S_i^\gamma S_j^\gamma\right),$$

where $J = (\lambda_\alpha + \lambda_\beta)/2$ represents the isotropic nearest-neighbor exchange coupling in the $\alpha\beta$ plane and $K = \lambda_\alpha - J$ is the Kitaev anisotropic nearest-neighbor exchange-coupling parameter. Using these formulations, we can calculate the values of J and K for both monolayer and bilayer, as listed in Table VI.

TABLE VI. J and K in monolayer and bilayer MnSe$_2$.

Layer number	J (meV/Mn)	K (meV/Mn)
1L	8.75	0.11
2L	11.47	0.04

APPENDIX D: STACKING ORDER TUNABLE MAGNETIC GROUND STATES AND EASY-AXIS DIRECTIONS

We considered several common stacking orders (Fig. 7) in TMD materials [30]. As shown in Table VII, we found AA stacking is most energetically favored among all considered stacking orders with an energy difference of at least 4 meV/Mn. Stacking orders can effectively modulate the interlayer magnetic ground states (AC and AA^R stacking) and easy-axis direction (AB stacking).
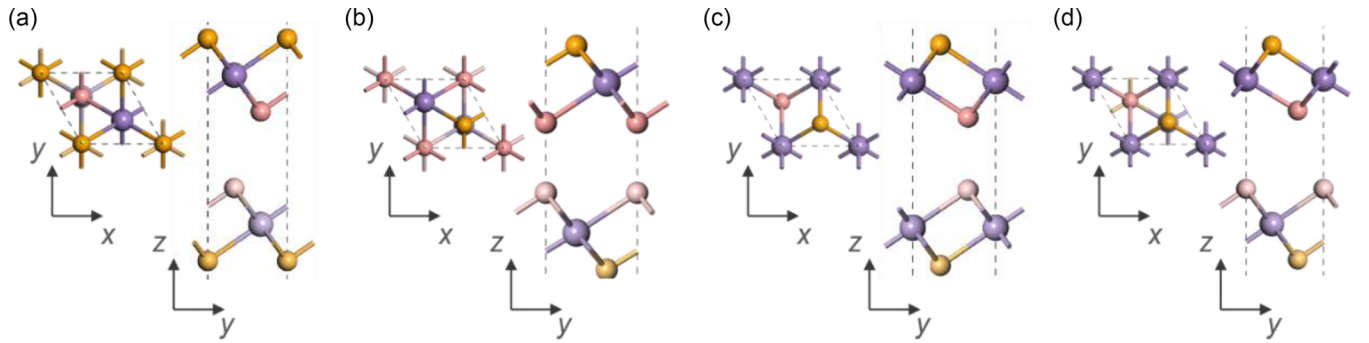

FIG. 7. Structure models of bilayer $MnSe_2$ in AB (a), AC (b), AA^R (c), and AB^R (d) stacking orders. We consider several common stacking orders in TMD materials [30].

TABLE VII. Magnetic properties and relative energy of bilayer $MnSe_2$ of stacking orders.

Stacking	Magnetic ground state	E (meV/Mn)	Easy axis	MAE (meV/Mn)
AA	FM-FM	0	Out of plane	0.6
AB	FM-FM	18	In plane	0.1
AC	FM-AFM	11	Out of plane	2.9
AA^R	FM-AFM	20	Out of plane	1.5
AB^R (same as AC^R)	FM-FM	4	Out of plane	0.7

APPENDIX E: *k*-MESH DEPENDENCE OF MAE CALCULATIONS

The magnetic anisotropy energy (MAE) is highly sensitive to the choice of k mesh. To ensure the accuracy of our calculations, we performed extensive convergence tests on the k mesh using the more accurate tetrahedron method with Blöchl corrections for total energy calculations. As shown in Fig. 8, E_x-E_z converges to 0.01 meV/Mn for both the monolayer and bilayer when the k mesh is set to 29×29. For atomically and orbitally decomposed MAE contributions, the k-point convergence is even better. These results ensure the robustness of the conclusions presented in our study.
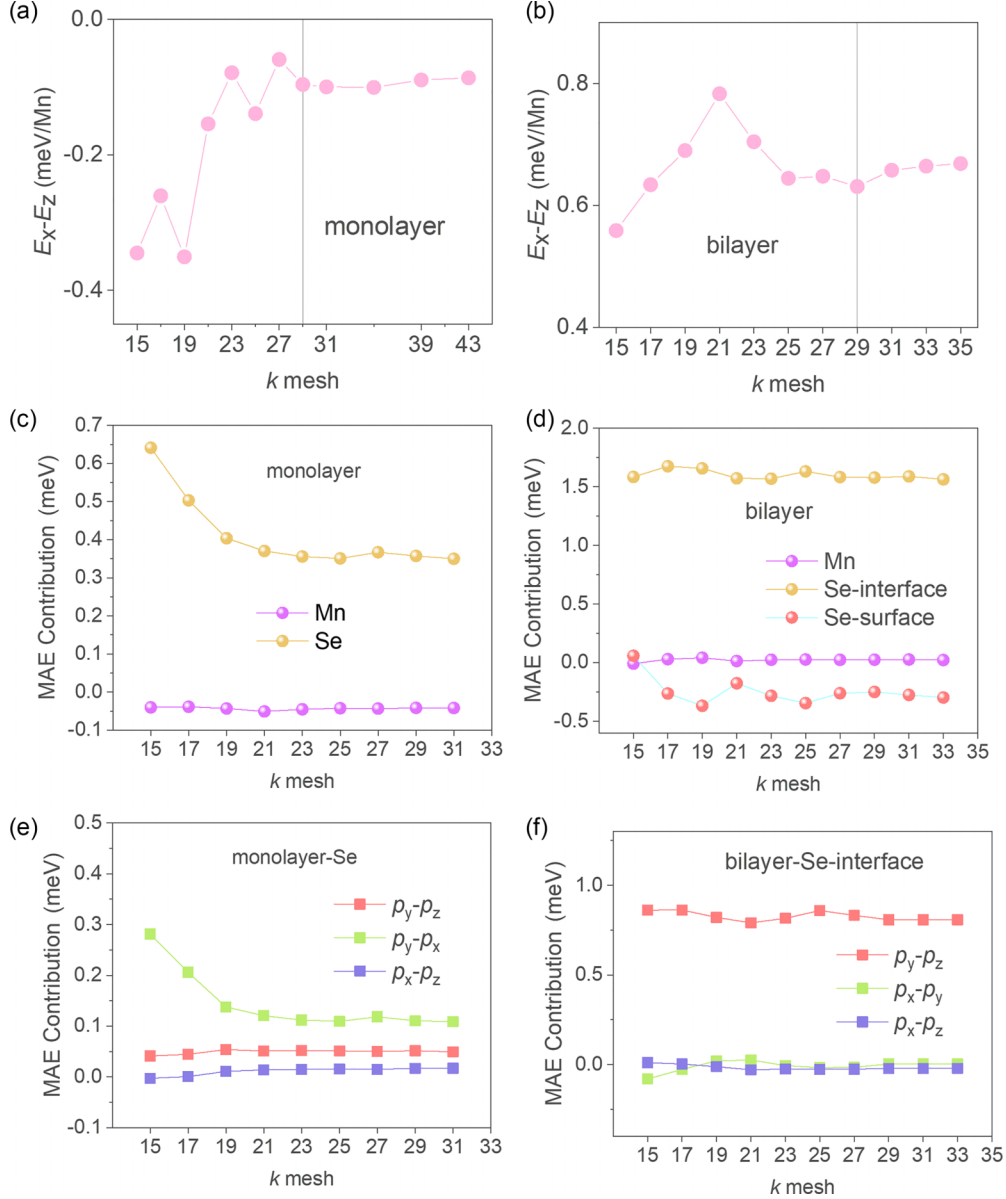

FIG. 8. (a), (b) Energy difference with respect to k mesh in monolayer (a) and bilayer (b), where E_x, E_z represent the energy of the magnetic moment along the directions of x- and z axes. (c)–(f) k-mesh dependence of atomically and orbitally decomposed MAE contributions.

APPENDIX F: ORBITAL-RESOLVED MAE CONTRIBUTIONS

We calculated orbital-resolved MAE contributions of Se in the monolayer and Se-surface in the bilayer, as shown in Fig. 9. In contrast to the monolayer, where all orbital components of Se atoms contribute positively to the MAE (Fig. 9(a)), the p_x-p_y and p_y-p_z components of the Se-surface atoms contribute to the MAE with opposite signs (Fig. 9(b)). Their competition leads to mutual cancellation, resulting in a weak and negative total MAE contribution from the Se-surface atoms.
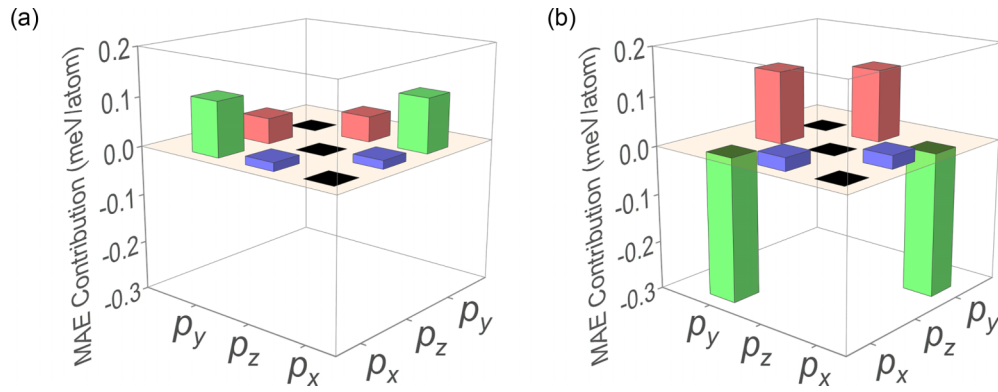

FIG. 9. Orbital-resolved MAE contribution of Se in monolayer (a) and Se surface in bilayer (b).
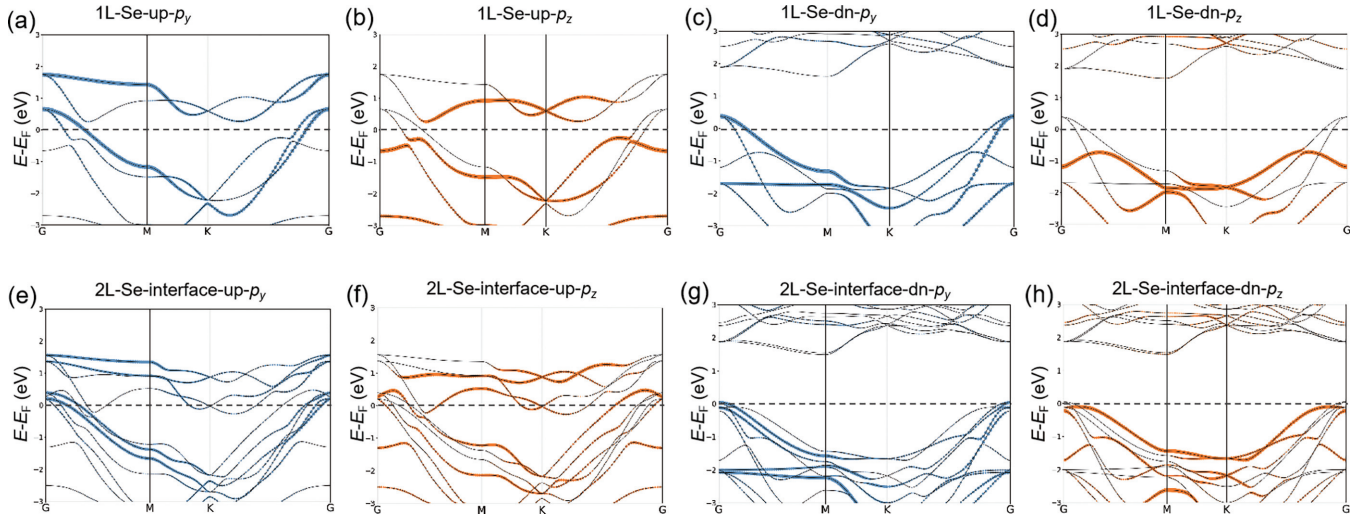
FIG. 10. Band structures of monolayer (a)–(d) and bilayer (e)–(h) MnSe$_2$. The (interfacial) Se p_z and p_y orbitals are mapped with different colors: orange, p_z; blue, p_y.

APPENDIX G: ELECTRONIC STRUCTURES WITH ORBITAL DECOMPOSITION

The states and their contributions to MAE can be related through the second-order perturbation theory [55]:

$$\text{MAE} = \sum_{u,o} \frac{|\langle u|H_{\text{SOC}}(x)|o\rangle|^2 - |\langle u|H_{\text{SOC}}(z)|o\rangle|^2}{E_o - E_u},$$

where o and u correspond to occupied and unoccupied states, respectively. The energy differences between occupied and unoccupied states (E_o-E_u) are in the denominator, indicating that states near the Fermi level have a greater influence on the MAE compared to those further away.

APPENDIX H: BAND STRUCTURES WITH THE INCLUSION OF SPIN-ORBIT COUPLING

We found that the change of magnetic moment direction can effectively regulate the electronic band structure and topological properties. After considering the spin-orbit coupling, three energy bands crossing the Fermi level as band $N - 1$, band N, and band $N + 1$, were selected to calculate their topological Chern numbers (marked with red, green and blue in Fig. 11).
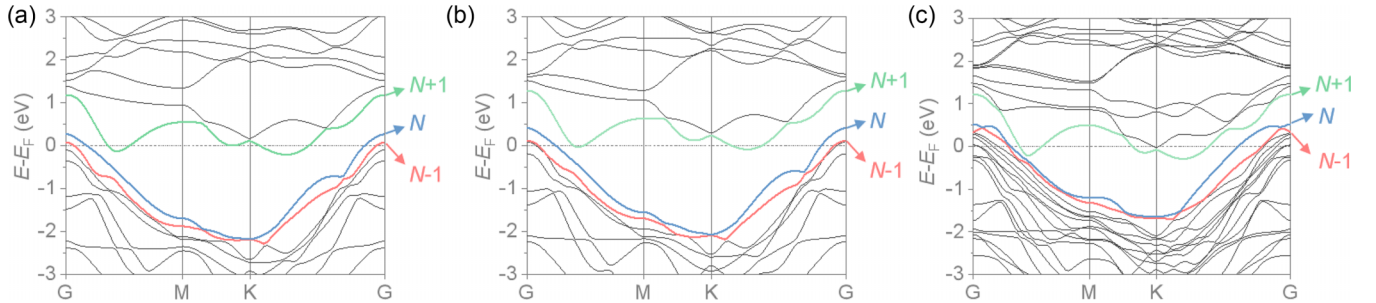

FIG. 11. Band structures of monolayer (a), (b) and bilayer (c) MnSe$_2$ with SOC, while the magnetic moment is along the easy axis of the monolayer in (a) and along the z axis in (b), (c). The symbols $N - 1$, N, $N + 1$ denote bands with respective colors.

APPENDIX I: EFFECTS OF STACKING ORDERS, DOPING, AND STRAIN ON EASY-AXIS DIRECTION

We found that charge doping (Table VIII), in-plane biaxial strain (Table IX), and stacking orders (Fig. 12) can effectively change the electron band structure around the Fermi level and thus the easy-axis direction.

TABLE VIII. Lattice constants, easy-axis direction, and magnetic anisotropic energies of monolayer $MnSe_2$ upon electron/hole doping. FM remains the ground state at different doping concentrations.

		Easy axis		
Electron doping (e/Se)	Lattice constant (Å)	θ(deg)	ϕ (deg)	E_x -E_{ea} (meV/Mn)
−0.1	3.58	90	90	0.01
−0.05	3.60	90	116	0.01
−0.0375	3.61	89	116	0.01
−0.025	3.61	90	112	0.01
0	3.61	68	111	0.01
0.05	3.61	17	96	0.29
0.075	3.61	0	90	0.74
0.1	3.63	0	90	0.81

TABLE IX. Lattice constants, easy-axis directions, and magnetic anisotropic energies of monolayer $MnSe_2$ under biaxial strain. FM remains the ground state under strain.

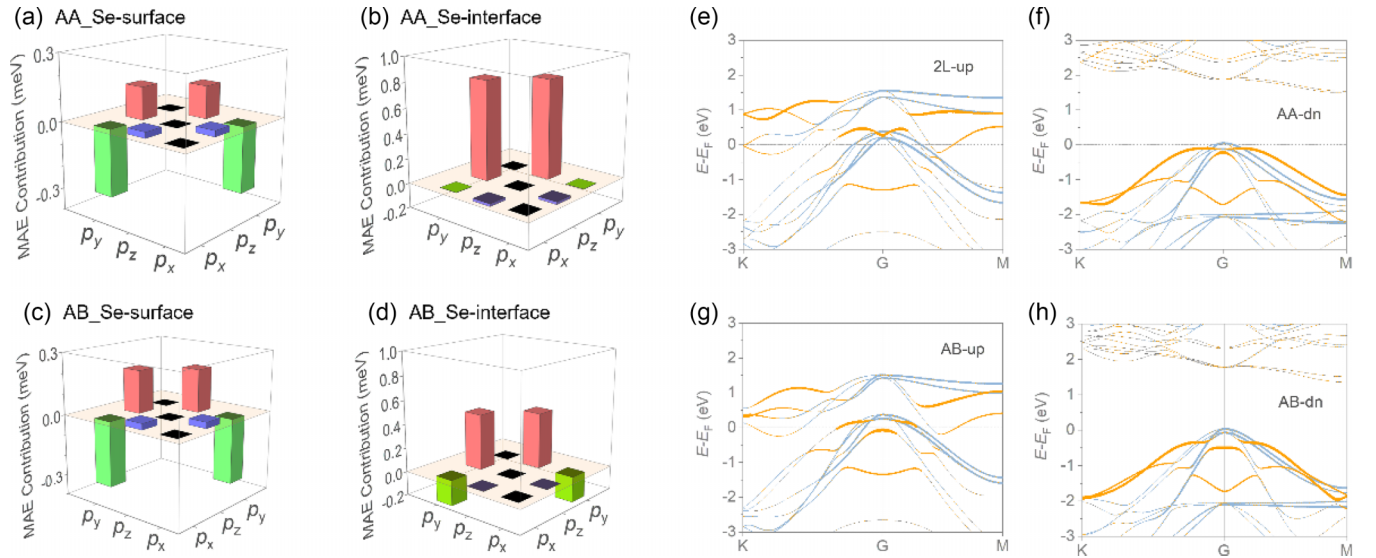|		Easy axis		
Strain (%)	Lattice constant (Å)	θ(deg)	ϕ (%)	$E_x - E_{ea}$ (meV/Mn)
−3	3.50	15	34	0.13
−2	3.54	0	90	0.29
−1	3.57	90	114	0.01
0	3.61	68	111	0.01
1	3.65	16	109	0.31
−3	3.68	0	90	0.93
−2	3.72	0	90	0.35

FIG. 12. Orbital-resolved MAE contribution of Se in AA (a), (b) and AB (c), (d) stacking. (e)–(h) Band structures of AA (e), (f) and AB (g), (h) stacked bilayer $MnSe_2$. The selected p_z and all p_y orbitals of (interfacial) Se are mapped with different colors: orange, p_z; light blue, p_y. The Fermi level is marked using a gray dotted-dashed line. From the orbital-resolved MAE in (a)–(d), we found that the most notable difference between AA and AB stacking lies in the weakened interaction between p_z and p_y states in AB stacking. This change arises from the shift of p_z states in AB-stacked bilayer.

[1] Q. H. Wang *et al.*, The magnetic genome of two-dimensional van der Waals materials, ACS Nano **16**, 6960 (2022).

[2] L. Nan-Shu, W. Cong, and J. Wei, Recent research advances in two-dimensional magnetic materials, Acta Phys. Sin. **71**, 127504 (2022).

[3] B. Huang *et al.*, Layer-dependent ferromagnetism in a van der Waals crystal down to the monolayer limit, Nature (London) **546**, 270 (2017).

[4] C. Gong *et al.*, Discovery of intrinsic ferromagnetism in two-dimensional van der Waals crystals, Nature (London) **546**, 265 (2017).

[5] B. Zhou, S. Ji, Z. Tian, W. Cheng, X. Wang, and W. Mi, Proximity effect induced spin filtering and gap opening in graphene by half-metallic monolayer Cr_2C ferromagnet, Carbon **132**, 25 (2018).

[6] C. Gong and X. Zhang, Two-dimensional magnetic crystals and emergent heterostructure devices, Science **363**, eaav4450 (2019).

[7] W. Vreugdenhil, J. G. Haasnoot, O. Kahn, P. Thuery, and J. Reedijk, A copper(II) dope as a detector for the high-spin.tautm. low-spin transition in the two-dimensional compound [trans-bis(thiocyanato)bis(4,4′-bi-1,2,4-triazole)iron] hydrate, J. Am. Chem. Soc. **109**, 5272 (1987).

[8] W. Liu, X. Bao, J.-Y. Li, Y.-L. Qin, Y.-C. Chen, Z.-P. Ni, and M.-L. Tong, High-temperature spin crossover in two solvent-free coordination polymers with unusual high thermal stability, Inorg. Chem. **54**, 3006 (2015).

[9] G. Chakraborty, I.-H. Park, R. Medishetty, and J. J. Vittal, Two-dimensional metal-organic framework materials: Synthesis, structures, properties and applications, Chem. Rev. **121**, 3751 (2021).

[10] J.-J. Xian *et al.*, Spin mapping of intralayer antiferromagnetism and field-induced spin reorientation in monolayer $CrTe_2$, Nat. Commun. **13**, 257 (2022).

[11] K. S. Burch, D. Mandrus, and J.-G. Park, Magnetism in two-dimensional van der Waals materials, Nature (London) **563**, 47 (2018).

[12] F. Yao, V. Multian, Z. Wang, N. Ubrig, J. Teyssier, F. Wu, E. Giannini, M. Gibertini, I. Gutiérrez-Lezama, and A. F. Morpurgo, Multiple antiferromagnetic phases and magnetic anisotropy in exfoliated $CrBr_3$ multilayers, Nat. Commun. **14**, 4969 (2023).

[13] Q. Cui, L. Wang, Y. Zhu, J. Liang, and H. Yang, Magnetic anisotropy, exchange coupling and Dzyaloshinskii—Moriya interaction of two-dimensional magnets, Front. Phys. **18**, 13602 (2023).

[14] Y. Wang *et al.*, Strain-sensitive magnetization reversal of a van der Waals magnet, Adv. Mater. **32**, 2004533 (2020).

[15] D. Chiba, M. Sawicki, Y. Nishitani, Y. Nakatani, F. Matsukura, and H. Ohno, Magnetization vector manipulation by electric fields, Nature (London) **455**, 515 (2008).

[16] I. M. Miron, K. Garello, G. Gaudin, P.-J. Zermatten, M. V. Costache, S. Auffret, S. Bandiera, B. Rodmacq, A. Schuhl, and P. Gambardella, Perpendicular switching of a single ferromagnetic layer induced by in-plane current injection, Nature (London) **476**, 189 (2011).

[17] X. Zhang *et al.*, Room-temperature intrinsic ferromagnetism in epitaxial $CrTe_2$ ultrathin films, Nat. Commun. **12**, 2492 (2021).

[18] L. Meng *et al.*, Anomalous thickness dependence of Curie temperature in air-stable two-dimensional ferromagnetic 1T-$CrTe_2$ grown by chemical vapor deposition, Nat. Commun. **12**, 809 (2021).

[19] M. Tsujikawa and T. Oda, Finite electric field effects in the large perpendicular magnetic anisotropy surface Pt/Fe/Pt(001): A first-principles study, Phys. Rev. Lett. **102**, 247203 (2009).

[20] B. Rana and Y. Otani, Towards magnonic devices based on voltage-controlled magnetic anisotropy, Commun Phys **2**, 1 (2019).

[21] C.-G. Duan, J. P. Velev, R. F. Sabirianov, Z. Zhu, J. Chu, S. S. Jaswal, and E. Y. Tsymbal, Surface magnetoelectric effect in ferromagnetic metal films, Phys. Rev. Lett. **101**, 137201 (2008).

[22] I. A. Verzhbitskiy, H. Kurebayashi, H. Cheng, J. Zhou, S. Khan, Y. P. Feng, and G. Eda, Controlling the magnetic anisotropy in $Cr_2Ge_2Te_6$ by electrostatic gating, Nat. Electron. **3**, 460 (2020).

[23] S. Jiang, L. Li, Z. Wang, K. F. Mak, and J. Shan, Controlling magnetism in 2D CrI_3 by electrostatic doping, Nat. Nanotechnol. **13**, 549 (2018).

[24] S. Jiang, J. Shan, and K. F. Mak, Electric-field switching of two-dimensional van der Waals magnets, Nat. Mater. **17**, 406 (2018).

[25] Y.-Y. Sun, L.-Q. Zhu, Z. Li, W. Ju, S.-J. Gong, J.-Q. Wang, and J.-H. Chu, Electric manipulation of magnetism in bilayer van der Waals magnets, J. Phys.: Condens. Matter **31**, 205501 (2019).

[26] T. Song *et al.*, Switching 2D magnetic states via pressure tuning of layer stacking, Nat. Mater. **18**, 1298 (2019).

[27] T. Li *et al.*, Pressure-controlled interlayer magnetism in atomically thin CrI_3, Nat. Mater. **18**, 1303 (2019).

[28] B. Huang, M. A. McGuire, A. F. May, D. Xiao, P. Jarillo-Herrero, and X. Xu, Emergent phenomena and proximity effects in two-dimensional magnets and heterostructures, Nat. Mater. **19**, 1276 (2020).

[29] X. Liu *et al.*, Tunable spin-polarized correlated states in twisted double bilayer graphene, Nature (London) **583**, 221 (2020).

[30] W. Zhu, C. Song, Y. Zhou, Q. Wang, H. Bai, and F. Pan, Insight into interlayer magnetic coupling in 1 T -type transition metal dichalcogenides based on the stacking of nonmagnetic atoms, Phys. Rev. B **103**, 224404 (2021).

[31] P. Jiang, C. Wang, D. Chen, Z. Zhong, Z. Yuan, Z.-Y. Lu, and W. Ji, Stacking tunable interlayer magnetism in bilayer CrI_3, Phys. Rev. B **99**, 144401 (2019).

[32] C. Wang, X. Zhou, Y. Pan, J. Qiao, X. Kong, C.-C. Kaun, and W. Ji, Layer and doping tunable ferromagnetic order in two-dimensional CrS_2 layers, Phys. Rev. B **97**, 245409 (2018).

[33] A. Avsar, A. Ciarrocchi, M. Pizzochero, D. Unuchek, O. V. Yazyev, and A. Kis, Defect induced, layer-modulated magnetism in ultrathin metallic $PtSe_2$, Nat. Nanotechnol. **14**, 674 (2019).

[34] J. Shang, X. Tang, X. Tan, A. Du, T. Liao, S. C. Smith, Y. Gu, C. Li, and L. Kou, Stacking-dependent interlayer magnetic coupling in 2D CrI_3 /$CrGeTe_3$ nanostructures for spintronics, ACS Appl. Nano Mater. **3**, 1282 (2020).

[35] B. Yang *et al.*, Magnetic anisotropy reversal driven by structural symmetry-breaking in monolayer α-$RuCl_3$, Nat. Mater. **22**, 50 (2023).

[36] J. P. Perdew, K. Burke, and M. Ernzerhof, Generalized gradient approximation made simple, Phys. Rev. Lett. **77**, 3865 (1996).

[37] P. E. Blöchl, Projector augmented-wave method, Phys. Rev. B **50**, 17953 (1994).

[38] G. Kresse and J. Furthmüller, Efficient iterative schemes for ab initio total-energy calculations using a plane-wave basis set, Phys. Rev. B **54**, 11169 (1996).

[39] S. Grimme, J. Antony, S. Ehrlich, and H. Krieg, A consistent and accurate *ab initio* parametrization of density functional dispersion correction (DFT-D) for the 94 elements H-Pu, J. Chem. Phys. **132**, 154104 (2010).

[40] N. Liu, C. Wang, C. Yan, C. Xu, J. Hu, Y. Zhang, and W. Ji, Competing multiferroic phases in monolayer and few-layer NiI$_2$, Phys. Rev. B **109**, 195422 (2024).

[41] A. I. Liechtenstein, V. I. Anisimov, and J. Zaanen, Density-functional theory and strong interactions: Orbital ordering in Mott-Hubbard insulators, Phys. Rev. B **52**, R5467 (1995).

[42] M. Cococcioni and S. de Gironcoli, Linear response approach to the calculation of the effective interaction parameters in the LDA+U method, Phys. Rev. B **71**, 035105 (2005).

[43] P. Li, X. Liu, M. Chen, P. Lin, X. Ren, L. Lin, C. Yang, and L. He, Large-scale *ab initio* simulations based on systematically improvable atomic basis, Comput. Mater. Sci. **112**, 503 (2016).

[44] M. Chen, G.-C. Guo, and L. He, Systematically improvable optimized atomic basis sets for *ab initio* calculations, J. Phys.: Condens. Matter **22**, 445501 (2010).

[45] G. Jin, H. Pang, Y. Ji, Z. Dai, and L. He, PYATB: An efficient Python package for electronic structure calculations using ab initio tight-binding model, Comput. Phys. Commun. **291**, 108844 (2023).

[46] A. A. Mostofi, J. R. Yates, G. Pizzi, Y.-S. Lee, I. Souza, D. Vanderbilt, and N. Marzari, An updated version of WANNIER90: A tool for obtaining maximally-localised Wannier functions, Comput. Phys. Commun. **185**, 2309 (2014).

[47] Q. Wu, S. Zhang, H.-F. Song, M. Troyer, and A. A. Soluyanov, WANNIERTOOLS: An open-source software package for novel topological materials, Comput. Phys. Commun. **224**, 405 (2018).

[48] W. Ji, Z.-Y. Lu, and H. Gao, Electron core-hole interaction and its induced ionic structural relaxation in molecular systems under x-ray irradiation, Phys. Rev. Lett. **97**, 246101 (2006).

[49] https://gitee.com/jigroupruc/re-meaf

[50] W.-Q. Xie, Z.-W. Lu, C.-C. He, X.-B. Yang, and Y.-J. Zhao, Theoretical study of tunable magnetism of two-dimensional MnSe$_2$ through strain, charge, and defect, J. Phys.: Condens. Matter **33**, 215803 (2021).

[51] C. Wang, X. Zhou, L. Zhou, Y. Pan, Z.-Y. Lu, X. Wan, X. Wang, and W. Ji, Bethe-Slater-curve-like behavior and interlayer spin-exchange coupling mechanisms in two-dimensional magnetic bilayers, Phys. Rev. B **102**, 020402(R) (2020).

[52] J. L. Lado and J. Fernández-Rossier, On the origin of magnetic anisotropy in two dimensional CrI$_3$, 2D Mater. **4**, 035002 (2017).

[53] D. Soriano, M. I. Katsnelson, and J. Fernández-Rossier, Magnetic two-dimensional chromium trihalides: A theoretical perspective, Nano Lett. **20**, 6225 (2020).

[54] Z. Wu, Z. Shen, Y. Xue, and C. Song, Strain-induced topological phase transition and enhanced Curie temperature in MnBi$_2$Te$_4$/CrI$_3$ heterojunction, Phys. Rev. Mater. **6**, 014011 (2022).

[55] D. Wang, R. Wu, and A. J. Freeman, First-principles theory of surface magnetocrystalline anisotropy and the diatomic-pair model, Phys. Rev. B **47**, 14932 (1993).

[56] S.-Z. Li, J.-S. Si, Z. Yang, and W.-B. Zhang, Weyl nodal loop semimetals and tunable quantum anomalous Hall states in two-dimensional ferromagnetic cerium monohalides, Phys. Rev. B **109**, 115418 (2024).

[57] L. Wu, L. Zhou, X. Zhou, C. Wang, and W. Ji, In-plane epitaxy-strain-tuning intralayer and interlayer magnetic coupling in CrSe$_2$ and CrTe$_2$ monolayers and bilayers, Phys. Rev. B **106**, L081401 (2022).